





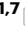


Efficient characterizations of multiphoton states with an ultra-thin optical device

Received: 13 June 2023

Accepted: 22 April 2024

Published online: 10 May 2024

 Check for updatesKui An ^{1,8}, Zilei Liu ^{2,3,8}, Ting Zhang¹, Siqi Li², You Zhou^{4,5}, Xiao Yuan ⁶,
Leiran Wang ^{2,3}, Wenfu Zhang ^{2,3}, Guoxi Wang ^{2,3} ✉ & He Lu ^{1,7} ✉

Metasurface enables the generation and manipulation of multiphoton entanglement with flat optics, providing a more efficient platform for large-scale photonic quantum information processing. Here, we show that a single metasurface optical device would allow more efficient characterizations of multiphoton entangled states, such as shadow tomography, which generally requires fast and complicated control of optical setups to perform information-complete measurements, a demanding task using conventional optics. The compact and stable device here allows implementations of general positive operator valued measures with a reduced sample complexity and significantly alleviates the experimental complexity to implement shadow tomography. Integrating self-learning and calibration algorithms, we observe notable advantages in the reconstruction of multiphoton entanglement, including using fewer measurements, having higher accuracy, and being robust against experimental imperfections. Our work unveils the feasibility of metasurface as a favorable integrated optical device for efficient characterization of multiphoton entanglement, and sheds light on scalable photonic quantum technologies with ultra-thin optical devices.

Metasurface, an ultra-thin and highly integrated optical device, is capable of full light control and thus provides novel applications in quantum photonics¹. In photonic quantum information processing, multiphoton entanglement is the building block for wide range of tasks, such as quantum computation², quantum error correction³, quantum secret sharing^{4,5}, and quantum sensing⁶. Recent investigations highlighted the feasibility of metasurface in generation^{7,8}, manipulation^{9–11}, and detection^{12,13} of multiphoton entanglement, indicating metasurface as a promising technology of ultra-thin optical device for large-scale quantum information processing.

Characterization of multiphoton entanglement provides diagnostic information on experimental imperfections and benchmarks

our technological progress towards the reliable control of large-scale photons. The standard quantum tomography (SQT)¹⁴ requires an exponential overhead with respect to the system size. Recently, more efficient protocols have been proposed and demonstrated with fewer measurements, such as compressed sensing^{15,16}, adaptive tomography^{17–19} and self-guided quantum tomography (SGQT)^{20–22}. Shadow tomography, which was first proposed by Aaronson et al.²³ and then concreted by Huang et al.²⁴, efficiently predicts functions of the quantum states instead of state reconstruction. Huang's protocol²⁴ is hereafter referred as shadow tomography. Shadow tomography is efficient in estimation of quantities in terms of observable (polynomial), including nonlinear observables such as purity and Rényi entropy^{25–28}, which is of particular interest in detecting multipartite

¹School of Physics, State Key Laboratory of Crystal Materials, Shandong University, Jinan 250100, China. ²State Key Laboratory of Transient Optics and Photonics, Xi'an Institute of Optics and Precision Mechanics, Chinese Academy of Sciences, Xi'an 710119, China. ³University of Chinese Academy of Sciences, Beijing 100049, China. ⁴Key Laboratory for Information Science of Electromagnetic Waves (Ministry of Education), Fudan University, Shanghai 200433, China. ⁵Hefei National Laboratory, Hefei 230088, China. ⁶Center on Frontiers of Computing Studies, Peking University, Beijing 100871, China. ⁷Shenzhen Research Institute of Shandong University, Shenzhen 518057, China. ⁸These authors contributed equally: Kui An, Zilei Liu. ✉ e-mail: wanguoxi@opt.ac.cn; luhe@sdu.edu.cn

entanglement^{29–32} and thus is helpful in benchmarking the technologies towards generation of genuine multipartite entanglement^{33–35}. Nevertheless, shadow tomography generally requires the experimental capability of performing information-complete measurements, leading to the consequence that the time of switching experimental setting is much longer than that of data acquisition. A potential solution is to replace the unitary operations and projective measurements with positive operator valued measures (POVMs), which is capable to extract complete information in a single experimental setting^{36–38}. The POVM significantly alleviates the experimental complexity to perform shadow tomography, and thus enables the real-time shadow tomography, i.e., an experimentalist is free to stop shadow tomography at any time. However, a compact and scalable implementation of POVM in optical system is still technically challenging. On the other hand, shadow tomography is not able to easily predict the properties that cannot be directly expressed in terms of observables (polynomial) such as von Neumann entropy $S(\rho) = -\text{Tr}(\rho \log \rho)$, which is key ingredient in topological entanglement entropy^{39,40}.

In this work, we report an implementation of POVM enabled by a metasurface, which is based on planar arrays of nanopillars and able to provide complete control of polarization. The POVM we achieved allows to implement real-time shadow tomography, and observe the shadow norm that determines sample complexity. Moreover, we show that the metasurface-enabled shadow tomography can be readily equipped with other algorithms, enabling the unexplored advantages of shadow tomography. In particular, we propose and implement shadow tomography optimized by simultaneous perturbation stochastic approximation (SPSA)⁴¹, the so-called self-learning shadow tomography (SLST). SLST efficiently returns a physical state with high accuracy against the metasurface-induced imperfections, which can be further used to calculate the quantities that cannot be expressed in terms of directly observable. We also implement robust shadow tomography⁴² to show the robustness of reconstruction against the engineered optical loss.

Results

Shadow tomography with POVM

We start by briefly reviewing the shadow tomography with POVM. Considering a 2-level (qubit) quantum system, a set of L rank-one projectors $\{|\psi_l\rangle\langle\psi_l| \in \mathbb{H}_2\}_{l=1}^L$ is called a quantum 2-design if the average value of the second-moment operator $(|\psi_l\rangle\langle\psi_l|)^{\otimes 2}$ over the set is proportional to the projector onto the totally symmetric subspace of two copies⁴³. Each quantum 2-design is proportional to a POVM $\mathbf{E} = \{\frac{2}{L}|\psi_l\rangle\langle\psi_l|\}_{l=1}^L$ with the element $E_l = \frac{2}{L}|\psi_l\rangle\langle\psi_l|$ being positive semi-definite and satisfying $\sum_{l=1}^L E_l = \mathbb{1}_2$. Note that quantum 1-design is sufficient to form a POVM but is not always information-complete for tomography, such as the measurement on computational basis $\{|0\rangle, |1\rangle\}$. Measuring a quantum state ρ using POVM \mathbf{E} results one $l \in [L]$ outcome with probability $\text{Pr}(l|\rho) = \text{Tr}(E_l\rho)$ according to Born's rule. The POVM \mathbf{E} together with the preparation of the corresponding state $|\psi_l\rangle$ can be viewed as a linear map $\mathcal{M} : \mathbb{H}_2 \rightarrow \mathbb{H}_2$, and the 'classical shadow' is the solution of least-square estimator with single experimental run,

$$\hat{\rho}_l^{(m)} = \mathcal{M}^{-1}(|\psi_l\rangle\langle\psi_l|) = 3|\psi_l\rangle\langle\psi_l| - \mathbb{1}_2. \quad (1)$$

For an N -qubit state, the classical shadow is the tensor product of simultaneous single-qubit estimations $\hat{\rho}^{(m)} = \bigotimes_{n=1}^N \hat{\rho}_n^{(m)}$ with l_n being the outcome of n -th qubit, and one has $\mathbb{E}[\hat{\rho}^{(m)}] = \rho$. Repeating the POVM M times (experimental runs), one has a collection of classical shadows $\{\hat{\rho}^{(m)}\}_{m=1}^M$, which is further inquired for estimation of various properties of the underlying state. See Supplementary Note 1A for more details.

Implementation of POVM with metasurface

In our experiment, we focus on the POVM on polarization-encoded qubit, i.e., $|0(1)\rangle = |H(V)\rangle$ with $|H(V)\rangle$ being the horizontal (vertical) polarization, and consider POVM of $L=6$ and $|\psi_l\rangle \in \{|H\rangle, |V\rangle, |+\rangle, |-\rangle, |R\rangle, |L\rangle\}$ with $|\pm\rangle = (|H\rangle \pm |V\rangle)/\sqrt{2}$ and $|R(L)\rangle = (|H\rangle \pm i|V\rangle)/\sqrt{2}$. The corresponding POVM \mathbf{E}_{octa} is described by a symmetric polytope of an octahedron on Bloch sphere as shown in Fig. 1a. To realize \mathbf{E}_{octa} , we

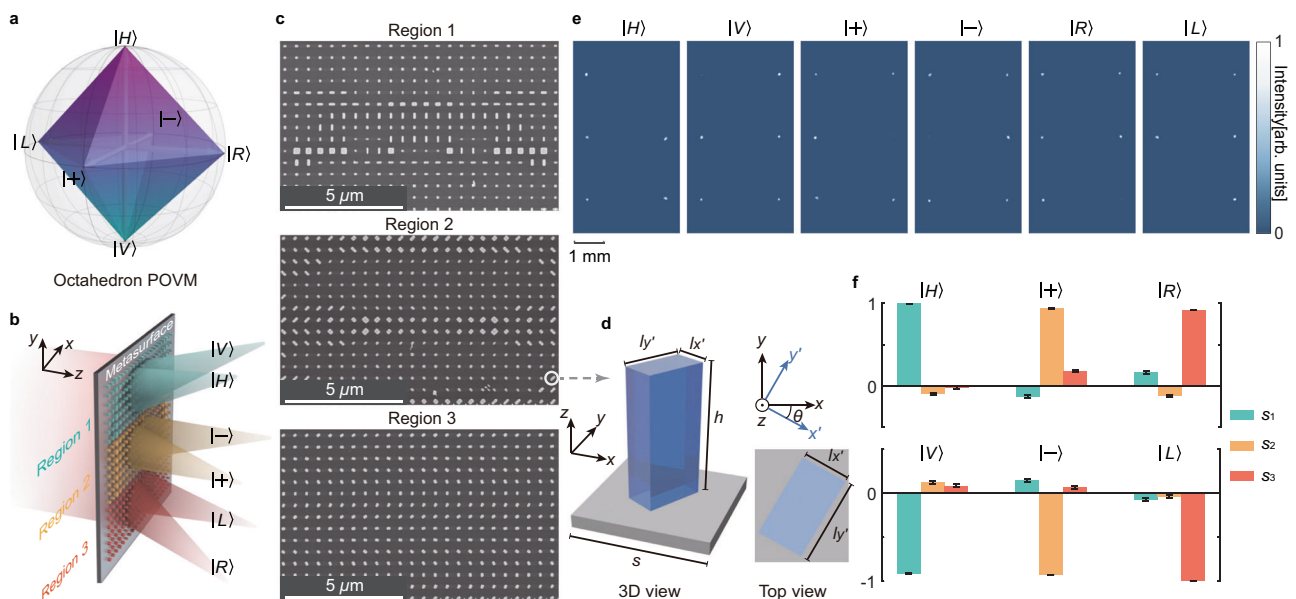


Fig. 1 | The metasurface-enabled octahedron positive operator valued measure (POVM) \mathbf{E}_{octa} . **a** The elements in \mathbf{E}_{octa} are projectors on states $|H\rangle$, $|V\rangle$, $|+\rangle$, $|-\rangle$, $|R\rangle$ and $|L\rangle$ respectively, which form a symmetric polytope of an octahedron on Bloch sphere. **b** The metasurface to realize \mathbf{E}_{octa} , green, yellow and red blocks on the metasurface represent nanopillars with different arrangements. **c** The scanning electron microscopy images of the fabricated nanopillars in three

regions. **d** Schematic drawing of single nanopillar that is fabricated with same height of 700 nm but different (θ, l_x, l_y) . **e** The measured distribution of intensity on focal plane with input polarization of $|H\rangle$, $|V\rangle$, $|+\rangle$, $|-\rangle$, $|R\rangle$ and $|L\rangle$, respectively. **f** The reconstructed Stokes parameters (s_1, s_2, s_3) from data collected in (e) and the error bars indicate standard deviations of reconstructed Stokes parameters.

design and fabricate a $210\ \mu\text{m} \times 210\ \mu\text{m}$ polarization-dependent metasurface that splits incident light into six directions corresponding to projection on $|H\rangle, |V\rangle, |+\rangle, |-\rangle, |R\rangle$ and $|L\rangle$ with equal probability (shown in Fig. 1b). Note that projection on $|\psi_l\rangle$ with equal probability is guaranteed with post-selection to eliminate the mode mismatch between incident light (Gaussian beam) and metasurface (square) (see Supplementary Note 5 for details). The metasurface is an array (with square pixel of $s = 500\ \text{nm}$) of single-layer amorphous silicon nanopillars on quartz substrate as shown in Fig. 1c, d. The nanopillars are with the same height of $700\ \text{nm}$ but different L_x, L_y and orientation θ relative to the reference coordinate system. In this sense, a single nanopillar can be regarded as a waveguide with different rectangular cross profile that exhibits corresponding effective birefringence, leading to spatial separation between orthogonal polarizations⁴⁴. The metasurface is divided into three regions with same size of $210\ \mu\text{m} \times 70\ \mu\text{m}$ but different arrangement of nanopillars, i.e., (θ, L_x, L_y) . By carefully designing the arrangement of nanopillars, we can realize spatial separation of $|H\rangle/|V\rangle, |+\rangle/|-\rangle$ and $|R\rangle/|L\rangle$, respectively. To validate the capability of fabricated metasurface to perform information-complete measurement, we test metasurface with input states of $|\psi_l\rangle$ and measure the distribution of output intensity on focal plane. The results are shown in Fig. 1e, according to which we reconstruct the Stokes parameters (s_1, s_2, s_3) shown in Fig. 1f. Compared to the ideal values, the average errors of reconstructed Stokes parameters are $0.101 \pm 0.005, 0.086 \pm 0.005$ and 0.073 ± 0.005 , respectively. These errors are mainly caused by the discretization of phase front in design, which inevitably introduces higher-order deflections⁴⁵ (see Supplementary Note 4 for details of metasurface).

Estimation of observables

We first perform shadow tomography with the fabricated metasurface on single-photon pure state $|\psi_{\gamma,\phi}\rangle = \cos\gamma|H\rangle + \sin\gamma e^{i\phi}|V\rangle$ with $\gamma = 0.91$ and $\phi = 0.12$. As shown in Fig. 2a, the polarization-entangled photons (central wavelength of $810\ \text{nm}$) are generated from a periodically poled potassium titanyl phosphate (PPKTP) crystal placed in a Sagnac interferometer via spontaneous parametric down conversion (SPDC), which is pumped by a laser diode (central wavelength of 405

nm). The generated entangled photons are with ideal form of $|\psi\rangle_\eta = \sqrt{\eta}|HV\rangle + \sqrt{1-\eta}|VH\rangle$, where η is determined by polarization of pump light. Projecting one photon of $|\psi\rangle_\eta$ on $|H\rangle$ heralds the other photon on state $|V\rangle$, which can further be transformed to arbitrary $|\psi_{\kappa,\nu}\rangle = \cos\kappa|H\rangle + \sin\kappa e^{i\nu}|V\rangle$ by a combination of electrically-rotated half-wave plate (E-HWP) and quarter-wave plate (E-QWP). Then, the heralded photon passes through the metasurface, and is coupled to six multimode fibers at outputs using an objective lens (OL), a tube lens, and three prisms, respectively. With the collection of classical shadows $\{\hat{\rho}^{(m)}\}_{m=1}^M$, we focus on the estimation of observables in set of 128 single-qubit projections, i.e., $O = |\psi_{\kappa,\nu}\rangle\langle\psi_{\kappa,\nu}| \in \mathbf{O}$ with $|\psi_{\kappa,\nu}\rangle = \cos\kappa|H\rangle + \sin\kappa e^{i\nu}|V\rangle$ being uniformly distributed on Bloch sphere. The estimation of expected value of observable is $\hat{O} = 1/M \sum_{m=1}^M \hat{o}^{(m)}$, where $\hat{o}^{(m)} = \text{Tr}(O\hat{\rho}^{(m)})$ is the i.i.d single-shot estimator. Note that \hat{O} converges to the exact expectation value $\langle O \rangle = \langle \psi_{\gamma,\phi} | O | \psi_{\gamma,\phi} \rangle$. As shown in Fig. 2b, the maximal distance $\max_{\mathbf{O}} \|\hat{O} - \langle O \rangle\|$ converges to 0.07 with the increase of M , which is consistent with the error we obtained in reconstruction of Stokes parameters. In Fig. 2c, we show the real-time estimation of \hat{O} by randomly selecting five $O \in \mathbf{O}$, in which we observe the convergence of \hat{O} after a few hundreds of milliseconds.

The sample complexity of estimation is further characterized by the variance $\text{Var}(\hat{O}) = \text{Var}(\hat{o}) \leq \|O\|_{\text{shd}}^2$. Here the shadow norm $\|O\|_{\text{shd}}^2$ ²⁴ is the maximization of $\text{Var}(\hat{o})$ over all possible states ρ to remove the state-dependence. For ideal \mathbf{E}_{Octa} , the shadow norm $\|O\|_{\text{shd}}^2 = 0.75$ regardless of the explicit form of $O \in \mathbf{O}$ (see Supplementary Note 1D for deviation of $\|O\|_{\text{shd}}^2 = 0.75$). Experimentally, the variance of a single-shot estimation is

$$\text{Var}(\hat{o}) = \frac{1}{M} \sum_{m=1}^M (\hat{o}^{(m)} - \hat{O})^2. \quad (2)$$

It is impossible to maximize $\text{Var}(\hat{o})$ over all possible $|\psi_{\gamma,\phi}\rangle$ in experiment, so that we prepare totally 20 $|\psi_{\gamma,\phi}\rangle$ that are uniformly distributed on Bloch sphere, forming a state set of \mathbf{P} . For each prepared

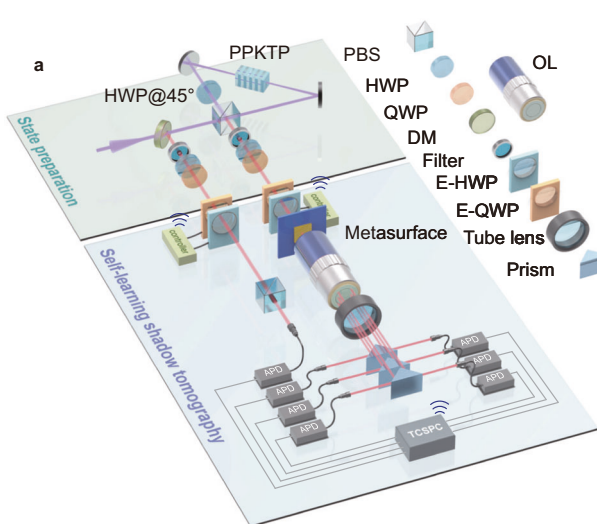
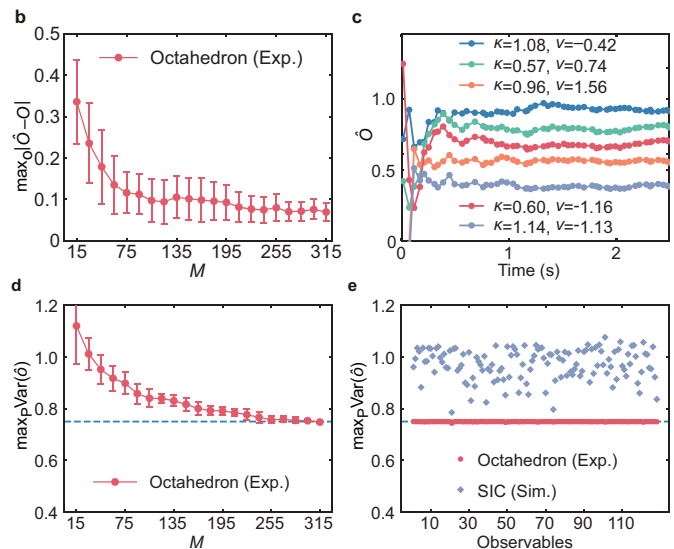


Fig. 2 | The experimental setup and results of shadow tomography with metasurface-enabled positive operator valued measure (POVM). **a** Setup to generate entangled photons and demonstrate shadow tomography with metasurface. PBS: polarizing beam splitter. DM: dichroic mirror. HWP: half-wave plate. QWP: quarter-wave plate. E-HWP: electrically-rotated HWP. E-QWP: electrically-rotated QWP. OL: objective lens. **b** The maximal error in estimation of expectation of $O \in \mathbf{O}$. **c** The real-time estimation of expectation of five randomly selected $O \in \mathbf{O}$. **d** The



results of shadow norm $\max_{\mathbf{O}} \text{Var}(\hat{o})$ for $O = |+\rangle\langle+|$ with different experimental runs. **e** The results of shadow norm for 128 $O \in \mathbf{O}$ (red dots), and the simulated results of shadow norm with symmetric informationally complete (SIC) POVM (blue diamonds). The 128 observables $O \in \mathbf{O}$ are selected according to Haar random. The dots and bars in **(b)** and **(d)** are the mean value and corresponding standard deviations obtained by repeating the experiment 5 times. The abbreviations of Exp. and Sim. indicate experimental results and simulation results respectively.

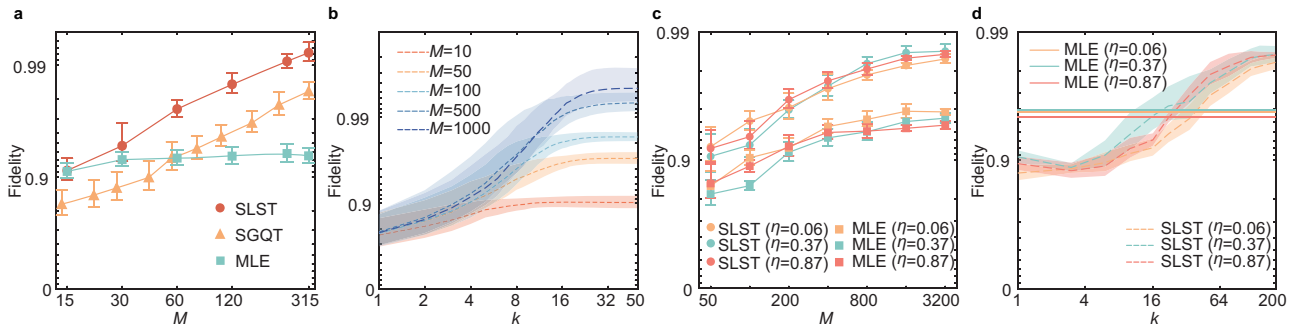


Fig. 3 | Experimental results of self-learning shadow tomography (SLST) on one-photon and two-photon states. **a** The average fidelity between reconstructed single-photon states τ and target state $|\psi\rangle_{y,\phi}$ using SLST, self-guided quantum tomography (SGQT), maximum likelihood estimation (MLE) reconstruction. **b** Average fidelity of SLST by increasing experimental runs M from 10 to 1000. **c** Fidelity between reconstructed two-photon states τ and target state ρ_η using SLST

and MLE. **d** The fidelities of two-photon states reconstruction from SLST (dash lines) with $M = 2000$ measurements. The solid lines represent the fidelity from MLE tomography with $M = 2000$ measurements. The dots and bars in (a) and (c) are the mean value and the corresponding standard deviations obtained by repeating the experiment 5 times. The dashed lines and shadings in (d) and (e) are the mean value and standard deviation obtained by repeating the iteration 5 times.

$|\psi_{y,\phi}\rangle$, we perform shadow tomography and estimate the expectation of $O = |+\rangle\langle +|$. The results of $\max_{\mathbf{p}} \text{Var}(\hat{o})$ are shown in Fig. 2d, in which we observe that $\max_{\mathbf{p}} \text{Var}(\hat{o}^{(m)})$ converges to 0.75 when $M > 255$. In Fig. 2e, we show $\max_{\mathbf{p}} \text{Var}(\hat{o})$ of 128 observables $O \in \mathbf{O}$ with $M = 315$ measurements, which agrees well with the theoretical prediction that the shadow norm is a constant regardless of the explicit form of $O \in \mathbf{O}$ ³⁸. To give a comparison, we simulate $\max_{\mathbf{p}} \text{Var}(\hat{o})$ with symmetric informationally complete (SIC) POVM \mathbf{E}_{SIC} ⁴⁶, which is constructed with the minimal number of 4 measurements for qubit system and has been widely adopted in investigations of advanced tomography^{47–49}. As shown in Fig. 2e, the shadow norm with \mathbf{E}_{SIC} depends on observable O and generally larger than that with \mathbf{E}_{Octa} , which indicates \mathbf{E}_{Octa} requires less shots M than \mathbf{E}_{SIC} to achieve the same accuracy of estimation \hat{O} .

State reconstruction

The direct estimation from classical shadows $\hat{\rho}^{(m)}$, i.e., $\hat{\rho} = 1/M \sum_{m=1}^M \hat{\rho}^{(m)}$, is generally not a physical state with finite M measurements, which limits the application of shadow tomography in estimation of nonlinear functions^{37,50}. Physical constraints need to be introduced to enforce the positivity of the reconstructed state τ , which can be addressed by solving the optimization problem

$$\begin{aligned} &\text{minimize} \quad \hat{N}_F(\tau) = \frac{2}{M(M-1)} \sum_{m < n} \text{Tr}[\hat{\rho}^{(m)} \hat{\rho}^{(n)}] + \text{Tr}(\tau^2) - 2 \sum_m \text{Tr}(\hat{\rho}^{(m)} \tau) \\ &\text{subject to} \quad \tau \geq 0, \text{Tr}(\tau) = 1, \end{aligned} \tag{3}$$

where τ is the proposed state that is positive semidefinite ($\tau \geq 0$) with unit trace ($\text{Tr}(\tau) = 1$), and the cost function $\hat{N}_F(\tau)$ is the unbiased estimator of squared Frobenius norm with $\{\hat{\rho}^{(m)}\}$ (see Supplementary Note 2A for more details). Note that the squared state fidelity adopted in SGQT^{20–22} is not an unbiased estimator with $\{\hat{\rho}^{(m)}\}$ for mixed state. We employ an iterative self-learning algorithm, i.e., SPSA algorithm, to solve the optimization problem in Eq. (3). SPSA is especially efficient in multi-parameter optimization problems in terms of providing a good solution for a relatively small number of measurements of the objective function⁵¹, which holds the similar spirit as shadow tomography. In traditional maximum likelihood estimation (MLE) reconstruction¹⁴, the computational expense required to estimate gradient direction is directly proportional to the number of unknown parameters ($4^N - 1$ for an N -qubit state) as it approximates the gradient by varying one parameter at a time, which becomes an issue when the number of qubit is large. In SPSA, the minimization of cost function $\hat{N}_F(\tau)$ is achieved by perturbing all parameters simultaneously, and one gradient evaluation requires only two evaluations of the cost function. While SPSA costs more iterations to converge, it returns state with higher fidelity in

limited number of iterations compared to MLE²¹. More importantly, SPSA formally accommodates noisy measurements of the objective function, which is an important practical concern in experiment.

Generally, an N -qubit state τ can be modeled with d^2 parameters with $d = 2^N$ being the dimension of τ . Thus, the proposed state τ is determined by a d^2 -dimensional vector $\mathbf{r} = [r_1, r_2, \dots, r_{d^2}]$. SPSA optimization estimates the gradient by simultaneously perturbing all parameters r_i in a random direction, instead of individually addressing each r_i . In k th iteration, the simultaneous perturbation approximation has all elements of \mathbf{r}_k perturbed together by a random perturbation vector $\mathbf{\Delta}_k = [\Delta_{k1}, \Delta_{k2}, \dots, \Delta_{kd^2}]$ with Δ_{ki} being generated from Bernoulli ± 1 distribution with equal probability. Then the gradient is calculated by

$$\mathbf{g}_k = \frac{\hat{N}_F(\mathbf{r}_k + B_k \mathbf{\Delta}_k) - \hat{N}_F(\mathbf{r}_k - B_k \mathbf{\Delta}_k)}{2B_k} \mathbf{\Delta}_k, \tag{4}$$

and \mathbf{r}_k is updated to \mathbf{r}_{k+1} by $\mathbf{r}_{k+1} = \mathbf{r}_k + A_k \mathbf{g}_k$. A_k and B_k are functions in forms of $A_k = a_1 / (k + a_2)^{a_3}$ and $B_k = b_1 / k^{b_2}$ with a_1, a_2, a_3, b_1 and b_2 being hyperparameters that determine the convergence speed of algorithm, which can be generally obtained from numerical simulations (see Supplementary Note 2B for hyperparameter settings). SLST is terminated when there is little change of $\hat{N}_F(\mathbf{r}_k)$ in several successive iterations, and corresponding τ_k is the reconstructed state. We emphasize that SPSA inevitably introduces systematic errors of the reconstructed state, as well as other optimization algorithms such as MLE and least squares⁵². In fact, it is a tradeoff that the reconstruction of a physical state suffers from a bias.

As the prepared single-photon state is extremely closed to the ideal state $|\psi_{y,\phi}\rangle$, the accuracy of reconstruction is characterized by the state fidelity between returned state τ_k and ideal state $|\psi_{y,\phi}\rangle$, i.e., $F = \sqrt{\text{Tr}(\tau_k |\psi_{y,\phi}\rangle \langle \psi_{y,\phi}|)}$. The results of average fidelity of SLST over 20 prepared $|\psi_{y,\phi}\rangle \in \mathbf{P}$ after $k = 30$ iterations are shown with red dots in Fig. 3a, where the average fidelity increases as M increases and achieves 0.992 ± 0.001 with $M = 315$ measurements. The fabricated metasurface is also capable to collect data required for state reconstruction with other technologies, i.e., SGQT^{20–22} and MLE reconstruction (see Supplementary Note 3 for demonstration of SGQT). In SGQT, two projective measurements are performed with 7 experimental runs in each iteration, and SPSA is used to update the proposed state τ^{SGQT} . The results of $F = \sqrt{\text{Tr}(\tau^{\text{SGQT}} |\psi_{y,\phi}\rangle \langle \psi_{y,\phi}|)}$ are shown with yellow triangles in Fig. 3a, in which we observe an average fidelity of 0.983 ± 0.003 after 45 iterations (total experimental runs of 315 as the same as that in SLST). The results of MLE reconstruction $F = \sqrt{\text{Tr}(\tau^{\text{MLE}} |\psi_{y,\phi}\rangle \langle \psi_{y,\phi}|)}$ are

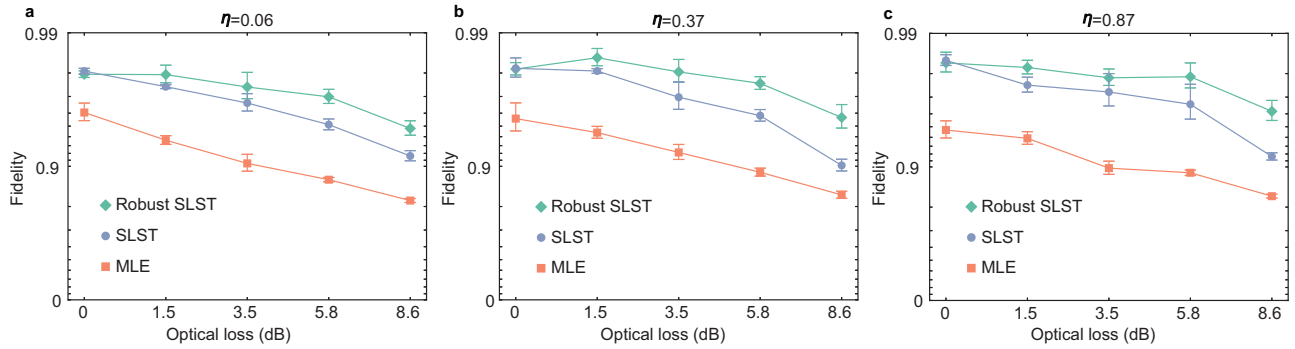


Fig. 4 | Results of fidelities from robust self-learning shadow tomography (SLST), SLST and maximum likelihood estimation (MLE) reconstruction on two-photon states. a $\rho_{\eta=0.06}$, **b** $\rho_{\eta=0.37}$ and **c** $\rho_{\eta=0.87}$. In each reconstructions, the experiment is carried out with $M=1000$ runs. In robust SLST, additional $M'=2000$

experimental runs are used for calibration. We set $k=200$ in robust SLST and SLST. The error bars are the standard deviations in SLST (robust SLST), obtained from Monte Carlo simulation with assumption that the collected photons in M (M' and M) experimental runs have Poisson distribution.

shown with cyan squares in Fig. 3a. When M is small ($M < 60$), MLE reconstruction is more accurate than SGQT. However, SLST always exhibits higher accuracy compared to other techniques with the same number of experimental runs. It is worth noting that the average fidelity with MLE reconstruction converges to 0.93 ± 0.01 and the error of reconstruction is about 0.07, which is consistent with errors in estimation of observables in Fig. 2b. Although the error of metasurface reduces the accuracy of shadow tomography and MLE reconstruction, SLST and SGQT with SPSA optimization can dramatically suppress metasurface-induced error as SPSA can accommodate noisy measurements of the cost function. The accuracy of SLST does not keep increasing with the number of iterations as reflected in Fig. 3b, where the converged fidelity depends on the number of experimental runs M in classical shadow collection.

We also demonstrate SLST on two-photon entangled states $|\psi\rangle_{\eta} = \sqrt{\eta}|HV\rangle + \sqrt{1-\eta}|VH\rangle$ with $\eta=0.06, 0.37$ and 0.87 . In two-photon SLST, one photon is detected by metasurface-enabled \mathbf{E}_{octa} , and the other photon is detected by randomly choosing σ_x , σ_y , and σ_z measurements realized by an E-HWP and an E-QWP. In contrast to the single-photon state, the generated two-photon state ρ_{η} is far from pure state as it is affected by more noises that are mainly attributed to high-order emission in SPDC and mode mismatch when overlapping two photons in Sagnac interferometer. Thus, the proposed state τ_k should be a mixed state in general form of $\tau_k = T^{\dagger}T$ with T being a complex lower triangular matrix (see Supplementary Note 2C for details). Accordingly, the accuracy of reconstruction is characterized by the fidelity between returned state τ_k and ρ_{η} , where ρ_{η} is MLE reconstruction with large amount of data ($M \approx 8 \times 10^5$) collected from bulk optical setting (waveplates and PBS). The results of $F = \text{Tr}(\sqrt{\sqrt{\tau_{200}}\rho_{\eta}\sqrt{\tau_{200}}})$ are shown with dots in Fig. 3c, the fidelities of three states reach 0.986 ± 0.002 , 0.990 ± 0.001 and 0.981 ± 0.002 with $M=2000$ experimental runs and $k=200$ iterations. We also perform MLE reconstruction τ^{MLE} of two-photon states, where one photon is detected by metasurface and the other is detected by bulk optical setting. The results of $F = \text{Tr}(\sqrt{\sqrt{\tau^{\text{MLE}}}\rho_{\eta}\sqrt{\tau^{\text{MLE}}}})$ with M experimental runs are shown with squares in Fig. 3c. The error in two-photon MLE reconstruction is about 0.047 ± 0.005 , which is smaller than that in single-photon MLE reconstruction as only one photon is detected by noisy device (metasurface). In Fig. 3d, we show that the fidelity of SLST with $M=2000$ is converging after $k=200$ iterations.

Robust shadow tomography

Finally, we demonstrate robustness of SLST can be further improved by robust shadow tomography^{42,53}. Considering that the measurement

apparatus are noisy, the measurement apparatus can be calibrated prior to performing SLST. To this end, shadow tomography is firstly performed on high-fidelity state $|HH\rangle$ with M' experimental runs to calculate the noisy quantum channel $\tilde{\mathcal{M}}$. Consequently, the classical shadow is constructed by the noisy channel, i.e., $\hat{\rho}^{(m)} = \tilde{\mathcal{M}}^{-1}(|\psi_{t_1}\rangle\langle\psi_{t_1}| \otimes |\psi_{t_2}\rangle\langle\psi_{t_2}|)$ (See Supplementary Note 1B for details of robust shadow tomography). The framework of robust shadow tomography is valid in our experimental setting. Firstly, although two photons are detected with different measurement devices, i.e., one is the metasurface-enabled POVM while the other is randomly detected on three Pauli bases, the mathematical models of these two measurement devices are identical. Secondly, although the metasurface-induced measurement errors are different between six projections, it has been shown that gate-dependent noise can be suppressed by robust shadow tomography⁴². Finally, the experimental device is able to generate $|HH\rangle$ with sufficiently high fidelity. Otherwise, the noise in state preparation might be added in $\tilde{\mathcal{M}}$, which introduces biased estimation of returned state. In our experiment, the fidelity of prepared $|HH\rangle$ is 0.9956 ± 0.0005 with respect to the ideal form. To demonstrate robust SLST, we insert a tunable attenuator before metasurface to introduce optical loss from 1.5 dB to 8.6 dB, which accordingly reduces the fidelity of prepared state as reflected by the MLE reconstruction shown in Fig. 4. Compared to SLST, robust SLST is able to enhance the accuracy of reconstruction in the presence of optical loss, especially at the high-level optical loss. It is worth mentioning that SLST itself can accommodate metasurface-induced measurement errors so that the enhancement of robust SLST is not significant when optical loss is zero. Increasing the optical loss is equivalent to stronger measurement noise. We observe the significant enhancement of robust SLST at high-level optical loss, which indicates robust SLST can further improve the robustness of SLST against noise (See Supplementary Note 1C for numerical simulations of robust SLST).

Discussion

We propose and demonstrate POVM with a single metasurface that enables implementation of real-time shadow tomography and observation of sample complexity. Together with the developed SLST, the underlying quantum states can be reconstructed efficiently, accurately and robustly. The advantages are evident even in single- and two-photon polarization-encoded states. The concept of octahedron POVM can be readily realized with integrated optics, where the directional couplers and phase shifters are able to construct octahedron POVM encoded in path degree of freedom. Metasurface-enabled POVM is particularly promising for efficient detection of scalable polarization-encoded multiphoton entanglement, in which two

measurement devices are sufficient for full characterization⁵⁴. Our investigation is compatible with metasurface-enabled generation^{7,8} and manipulation^{9–11} of photonic states, thereby opening the door to quantum information processing with a single ultra-thin optical device.

Methods

Fabrication of metasurface

A 700 nm-thick layer of a-Si is deposited on top of 750 μm -thick fused quartz wafers using the low-pressure chemical vapor deposition (LPCVD) technique. Then a layer of AR-P6200.09 resists (Allresist GmbH) with a thickness of 200 nm is spun and coated on the substrate. The metasurface pattern is generated with electron-beam lithography (EBL) process which is set with 120 kV, 1 nA current and 300 $\mu\text{C cm}^{-2}$ dose. Subsequently, the resist is developed with AR300-546 (Allresist GmbH) for 1 min. Reaction ion etching (RIE) is performed to transfer the nanostructures to a-Si film. The residue resist is removed by immersing the chip first in acetone for 5 min, then in isopropanol for 5 min and finally in deionized water.

Experimental setup to implement SLST with metasurface

Metasurface is fixed on a piece of hollow plastic, which can be adjusted in six degrees of freedom through a six-dimensional rotation stage. Objective lens with 20 \times magnifying factor and tube lens with the focal length of 200 mm is used as a microscope, enlarging the distance of six spots focused by metasurface from 70 μm to 1.9 mm. Then, three prisms at different heights are applied to separate six light beams. Four mini lenses with $f=15$ mm and two mini lenses with $f=30$ mm are used to couple the six beams into six multi-mode fibers with the core diameter of 62.5 μm .

Data availability

The data generated in this study have been deposited in the Zenodo database with the identifier <https://zenodo.org/records/10674374> [<https://doi.org/10.5281/zenodo.10674373>].

Code availability

The codes used for data analysis and simulation in this study have been deposited in the Zenodo database with the identifier <https://zenodo.org/records/10674374> [<https://doi.org/10.5281/zenodo.10674373>].

References

- Solntsev, A. S., Agarwal, G. S. & Kivshar, Y. S. Metasurfaces for quantum photonics. *Nat. Photonics* **15**, 327–336 (2021).
- Walther, P. et al. Experimental one-way quantum computing. *Nature* **434**, 169–176 (2005).
- Yao, X.-C. et al. Experimental demonstration of topological error correction. *Nature* **482**, 489–494 (2012).
- Bell, B. A. et al. Experimental demonstration of graph-state quantum secret sharing. *Nat. Commun.* **5**, 5480 (2014).
- Lu, H. et al. Secret sharing of a quantum state. *Phys. Rev. Lett.* **117**, 030501 (2016).
- Liu, L.-Z. et al. Distributed quantum phase estimation with entangled photons. *Nat. Photonics* **15**, 137–142 (2021).
- Li, L. et al. Metalens-array-based high-dimensional and multiphoton quantum source. *Science* **368**, 1487–1490 (2020).
- Santiago-Cruz, T. et al. Resonant metasurfaces for generating complex quantum states. *Science* **377**, 991–995 (2022).
- Georgi, P. et al. Metasurface interferometry toward quantum sensors. *Light Sci. Appl.* **8**, 70 (2019).
- Li, Q. et al. A non-unitary metasurface enables continuous control of quantum photon–photon interactions from bosonic to fermionic. *Nat. Photonics* **15**, 267–271 (2021).
- Zhang, D. et al. All-optical modulation of quantum states by nonlinear metasurface. *Light Sci. Appl.* **11**, 58 (2022).
- Wang, K. et al. Quantum metasurface for multiphoton interference and state reconstruction. *Science* **361**, 1104–1108 (2018).
- Wang, Z. et al. Implement quantum tomography of polarization-entangled states via nondiffractive metasurfaces. *Appl. Phys. Lett.* **121**, 081703 (2022).
- James, D. F. V., Kwiat, P. G., Munro, W. J. & White, A. G. Measurement of qubits. *Phys. Rev. A* **64**, 052312 (2001).
- Gross, D., Liu, Y.-K., Flammia, S. T., Becker, S. & Eisert, J. Quantum state tomography via compressed sensing. *Phys. Rev. Lett.* **105**, 150401 (2010).
- Liu, W.-T., Zhang, T., Liu, J.-Y., Chen, P.-X. & Yuan, J.-M. Experimental quantum state tomography via compressed sampling. *Phys. Rev. Lett.* **108**, 170403 (2012).
- Mahler, D. H. et al. Adaptive quantum state tomography improves accuracy quadratically. *Phys. Rev. Lett.* **111**, 183601 (2013).
- Hou, Z., Zhu, H., Xiang, G.-Y., Li, C.-F. & Guo, G.-C. Achieving quantum precision limit in adaptive qubit state tomography. *NPJ Quantum Inf.* **2**, 16001 (2016).
- Granade, C., Ferrie, C. & Flammia, S. T. Practical adaptive quantum tomography. *New J. Phys.* **19**, 113017 (2017).
- Ferrie, C. Self-guided quantum tomography. *Phys. Rev. Lett.* **113**, 190404 (2014).
- Chapman, R. J., Ferrie, C. & Peruzzo, A. Experimental demonstration of self-guided quantum tomography. *Phys. Rev. Lett.* **117**, 040402 (2016).
- Rambach, M. et al. Robust and efficient high-dimensional quantum state tomography. *Phys. Rev. Lett.* **126**, 100402 (2021).
- Aaronson, S. Shadow tomography of quantum states. In *Proceedings of the 50th Annual ACM SIGACT Symposium on Theory of Computing*. 325–338 (ACM, 2018).
- Huang, H.-Y., Kueng, R. & Preskill, J. Predicting many properties of a quantum system from very few measurements. *Nat. Phys.* **16**, 1050–1057 (2020).
- Brydges, T. et al. Probing rényi entanglement entropy via randomized measurements. *Science* **364**, 260–263 (2019).
- Elben, A. et al. Cross-platform verification of intermediate scale quantum devices. *Phys. Rev. Lett.* **124**, 010504 (2020).
- Garcia, R. J., Zhou, Y. & Jaffe, A. Quantum scrambling with classical shadows. *Phys. Rev. Research* **3**, 033155 (2021).
- Liu, Z., Zeng, P., Zhou, Y. & Gu, M. Characterizing correlation within multipartite quantum systems via local randomized measurements. *Phys. Rev. A* **105**, 022407 (2022).
- Elben, A. et al. Mixed-state entanglement from local randomized measurements. *Phys. Rev. Lett.* **125**, 200501 (2020).
- Zhou, Y., Zeng, P. & Liu, Z. Single-copies estimation of entanglement negativity. *Phys. Rev. Lett.* **125**, 200502 (2020).
- Neven, A. et al. Symmetry-resolved entanglement detection using partial transpose moments. *NPJ Quantum Inf.* **7**, 152 (2021).
- Zhang, T. et al. Experimental quantum state measurement with classical shadows. *Phys. Rev. Lett.* **127**, 200501 (2021).
- Lu, H. et al. Entanglement structure: entanglement partitioning in multipartite systems and its experimental detection using optimizable witnesses. *Phys. Rev. X* **8**, 021072 (2018).
- Zhou, Y., Zhao, Q., Yuan, X. & Ma, X. Detecting multipartite entanglement structure with minimal resources. *NPJ Quantum Inf.* **5**, 1–8 (2019).
- Zhou, Y. et al. A scheme to create and verify scalable entanglement in optical lattice. *NPJ Quantum Inf.* **8**, 99 (2022).
- Acharya, A., Saha, S. & Sengupta, A. M. Shadow tomography based on informationally complete positive operator-valued measure. *Phys. Rev. A* **104**, 052418 (2021).
- Stricker, R. et al. Experimental single-setting quantum state tomography. *PRX Quantum* **3**, 040310 (2022).

38. Nguyen, H. C., Bönsel, J. L., Steinberg, J. & Gühne, O. Optimizing shadow tomography with generalized measurements. *Phys. Rev. Lett.* **129**, 220502 (2022).
 39. Kitaev, A. & Preskill, J. Topological entanglement entropy. *Phys. Rev. Lett.* **96**, 110404 (2006).
 40. Satzinger, K. J. et al. Realizing topologically ordered states on a quantum processor. *Science* **374**, 1237–1241 (2021).
 41. Spall, J. Multivariate stochastic approximation using a simultaneous perturbation gradient approximation. *IEEE Trans. Automat. Contr.* **37**, 332–341 (1992).
 42. Chen, S., Yu, W., Zeng, P. & Flammia, S. T. Robust shadow estimation. *PRX Quantum* **2**, 030348 (2021).
 43. Guță, M., Kahn, J., Kueng, R. & Tropp, J. A. Fast state tomography with optimal error bounds. *J. Phys. A: Math. Theor.* **53**, 204001 (2020).
 44. Arbabi, A., Horie, Y., Bagheri, M. & Faraon, A. Dielectric metasurfaces for complete control of phase and polarization with sub-wavelength spatial resolution and high transmission. *Nanotechnol.* **10**, 937–943 (2015).
 45. Sell, D., Yang, J., Doshay, S., Yang, R. & Fan, J. A. Large-angle, multifunctional metagratings based on freeform multimode geometries. *Nano Lett.* **17**, 3752–3757 (2017).
 46. Renes, J. M., Blume-Kohout, R., Scott, A. J. & Caves, C. M. Symmetric informationally complete quantum measurements. *J. Math. Phys.* **45**, 2171–2180 (2004).
 47. Torlai, G. et al. Neural-network quantum state tomography. *Nat. Phys.* **14**, 447–450 (2018).
 48. Carrasquilla, J., Torlai, G., Melko, R. G. & Aolita, L. Reconstructing quantum states with generative models. *Nat. Mach. Intell.* **1**, 155–161 (2019).
 49. García-Pérez, G. et al. Learning to measure: adaptively informationally complete generalized measurements for quantum algorithms. *PRX Quantum* **2**, 040342 (2021).
 50. Zhou, Y. & Liu, Z. A hybrid framework for estimating nonlinear functions of quantum states. *arXiv* <https://arxiv.org/abs/2208.08416> (2022).
 51. Spall, J. C. *Introduction to Stochastic Search and Optimization: Estimation, Simulation, and Control*, (John Wiley & Sons, 2005).
 52. Schwemmer, C. et al. Systematic errors in current quantum state tomography tools. *Phys. Rev. Lett.* **114**, 080403 (2015).
 53. Koh, D. E. & Grewal, S. Classical shadows with noise. *Quantum* **6**, 776 (2022).
 54. Meyer-Scott, E. et al. Scalable generation of multiphoton entangled states by active feed-forward and multiplexing. *Phys. Rev. Lett.* **129**, 150501 (2022).
- vince (Grant No. tsqn202103013), Shenzhen Fundamental Research Program (Grants Nos. JCYJ20190806155211142 and JCYJ20220530141013029), Shandong University Multidisciplinary Research and Innovation Team of Young Scholars (Grant No. 2020QNQT) and Higher Education Discipline Innovation Project (‘111’ (Grant No. B13029). S. L. and G. W. were supported by the National Natural Science Foundation of China (Grants Nos. 62375282 and 62205370). Y. Z. was supported by the National Natural Science Foundation of China (Grants No. 12205048) and Innovation Program for Quantum Science and Technology (Grant No. 2021ZD0302000).

Author contributions

H.L. conceived and designed the experiment. K.A. T.Z. and H.L. carried out the experiment of SLST. Z.L., S.L., L.W., W.Z. and G.W. designed and fabricated metasurface. Y. Z., X. Y. and H. L. conducted the theoretical analysis. H. L. and G. W. supervised the project. All authors contributed to writing the manuscript.

Competing interests

The authors have no competing interests.

Additional information

Supplementary information The online version contains supplementary material available at <https://doi.org/10.1038/s41467-024-48213-4>.

Correspondence and requests for materials should be addressed to Guoxi Wang or He Lu.

Peer review information *Nature Communications* thanks the anonymous, reviewer(s) for their contribution to the peer review of this work. A peer review file is available.

Reprints and permissions information is available at <http://www.nature.com/reprints>

Publisher's note Springer Nature remains neutral with regard to jurisdictional claims in published maps and institutional affiliations.

Open Access This article is licensed under a Creative Commons Attribution 4.0 International License, which permits use, sharing, adaptation, distribution and reproduction in any medium or format, as long as you give appropriate credit to the original author(s) and the source, provide a link to the Creative Commons licence, and indicate if changes were made. The images or other third party material in this article are included in the article's Creative Commons licence, unless indicated otherwise in a credit line to the material. If material is not included in the article's Creative Commons licence and your intended use is not permitted by statutory regulation or exceeds the permitted use, you will need to obtain permission directly from the copyright holder. To view a copy of this licence, visit <http://creativecommons.org/licenses/by/4.0/>.

© The Author(s) 2024

Acknowledgements

The authors thank Xiaoqi Zhou for insightful discussion. The authors thank the anonymous reviewers for the insightful comments on the work. K. A., T. Z. and H. L. were supported by the National Key Research and Development Program of China (Grant No. 2019YFA0308200), the National Natural Science Foundation of China (Grants Nos. 11974213 and 92065112), Shandong Provincial Natural Science Foundation (Grant Nos. ZR2020JQ05 and ZR2023LLZ005), Taishan Scholar of Shandong Pro-